# 3-D Modeling of SCR of $NO_x$ by $NH_3$ on Vanadia Honeycomb Catalysts

**B. Roduit and A. Baiker**
Laboratory of Technical Chemistry, Swiss Federal Institute of Technology, ETH-Zentrum, CH-8092 Zurich, Switzerland

**F. Bettoni**
Institute of Process Engineering, Swiss Federal Institute of Technology, CH-8092 Zurich, Switzerland

**J. Baldyga**
Dept. of Chemical and Process Engineering, Warsaw University of Technology, PL-00-645 Warsaw, Poland

**A. Wokaun**
General Energy Research, Paul Scherrer Inst., CH-5232 Villigen, Switzerland

*A novel scheme for simulating the selective catalytic reduction of NO with $NH_3$ on a honeycomb-type catalyst was developed based on a 3-D model. New insight was gained by considering such modeling aspects as: correct geometry (square ducts); hydrodynamic entrance effects; occurrence of adsorption phenomena and side reactions; $NH_3$/NO ratio in the feed; influence of the reactant (NO, $NH_3$, $O_2$, $H_2O$) concentrations; intraphase diffusion and interphase mass-transfer processes; and a large range of operating conditions (temperature 140–475°C and gas hourly space velocity 14,800–73,900 $h^{-1}$). These aspects proved to be crucial for interpreting and quantifying the experimental results and optimizing the catalytic reactor processes. The 3-D model was validated by comparing manufacturer's set point and experimental data to calculated data, and the external mass-transfer coefficients derived from the concentration gradients to the mass-transfer correlations available in the literature.*

## Introduction

Due to the efficiency of the vanadia-based catalysts for the selective catalytic reduction of NO with $NH_3$ and their resistance to $SO_2$ poisoning, they have received much attention in recent years (e.g., Inomata et al., 1980; Topsoe, 1991, 1994; Srnak et al., 1992; Schneider et al., 1994; Duffy et al., 1994a,b; Ozkan et al., 1994; Topsoe et al., 1995a,b; Lietti et al., 1996; Hu and Apple, 1996; Pinaeva et al., 1996; Ramis et al., 1996; Dumesic et al., 1996; Gilardoni et al., 1997a,b; Kumthekar and Ozkan, 1997) and a great number of studies were performed to investigate the reaction mechanism. As regard has grown for the use of monoliths in selective catalytic reduction (SCR) to avoid emissions of nitrogen oxides ($NO_x$), so too has the requirement for the mathematical modeling of this reaction (Buzanowski and Yang, 1990; Beeckman and Hegedus, 1991; Tronconi and Forzatti, 1992; Heinisch et al., 1992; Bahamonde et al., 1996; Forzatti and Lietti, 1996; Tronconi, 1997; Bai and Chwu, 1997). Successful modeling of the real physicochemical processes occurring in monolith reactors requires, among other things, consideration of the proper geometry and all possible interacting effects in the mathematical description.

The aim of the present article is the quantification of the various aspects of the SCR of NO with $NH_3$, because in spite of the rapidly growing knowledge of the particular mechanisms, only a precise consideration and quantification of the phenomena taking place provide a reliable means for achieving maximal performance of the reactor for a given size, number and shape of the channel, and operating conditions such as temperature, gas hourly space velocity (GHSV), and pollutant concentrations.

The derivation of the kinetic expressions used in this work was reported in a detailed study of the global kinetics of the SCR reaction by Roduit et al. (1998).

Correspondence concerning this article should be addressed to A. Baiker.

## Experimental Studies

A detailed description of the experimental procedure that was used is given by Bettoni (1997), and the following subsections depict only the main experimental settings.

### *Diesel motor*

The exhaust gases used in the present work as a reactant for the SCR reaction were produced by a diesel motor (New Sulzer Diesel AG, Switzerland) characterized by the following parameters: motor (NSD, 9S20, type/displacement: nine cylinders in-line four-stroke engine with direct injection), bore $\times$ stroke ($200\times300$ mm), volume of one cylinder (9.5-L combustion chamber), performance (1.3-MW electric power from generator), fuel consumption ($\sim 200$ g/kWh), air consumption (about 8,000 $m^3$/h, 20°C, 1 bar), outlet flue-gas temperature ($\sim 450$°C), outlet flue-gas flow (about 7,600 $Nm^3$/h, approximately 20,000 $m^3$/h at 450°C, 1 bar). The composition of exhaust gases for a performance of 890 kW is given in Table 1.

### *Honeycomb*

The reactor contained four honeycomb elements (Hüls GmbH, Germany) with a cross section of $150\times150$ mm each and the following characteristics: geometry: honeycomb with square ducts; length: 580 mm; cross section: $150\times150$ mm; number of channels: $35\times35$; wall thickness: 0.78 mm; channel pitch: 3.45 mm; free cross section: 64.8%; geometric surface: 751 $m^2/m^3$; pore volume: 0.3 $cm^3$/g; specific surface: BET, 70 $m^2$/g; density: 500–670 kg/$m^3$; chemical composition: $TiO_2$— >70%; $V_2O_5$—5%; $WO_3$; $MoO_3$; and additives.

### *Ammonia injection system*

In the present study, ammonia was injected using aqueous ammonia solution containing 24 wt. % ammonia. A detailed description of the injection system used can be found in Bettoni (1997). The injection into the flue-gas stream through an atomizing nozzle was tested with and without mixer package (Sulzer, Switzerland) at two different locations, 1.4 and 3.4 m, respectively, upstream of the SCR reactor. In addition, four different operating methods were examined for the injection of ammonia into the flue gas:

1. axial injection with flow
2. axial injection with flow without compressed air
3. counterflow axial injection
4. radial injection perpendicular to flow.

At 3.4 m upstream, (3), the counterflow axial injection, and (1), axial injection with flow, did not show any noticeable differences in the NO conversion and $NH_3$ slip, and thus ensured a proper distribution of both flue gas and reductant.

## General Description of the Model

The investigation of heterogeneous catalytic reactions and catalytic processes is complicated by the fact that it usually involves diffusion and chemical phenomena, which are not easy to separate in order to identify the factors that affect each of them. Many authors (Beeckman and Hegedus, 1991; Tronconi and Forzatti, 1992; Tronconi et al., 1992; Heinisch et al., 1992; Bahamonde et al., 1996; Forzatti and Lietti, 1996; Tronconi, 1997) have described the transport phenomena using derived mass-transfer correlations for a laminar parabolic velocity profile in a tube, taking the hydraulic diameter as the characteristic length when different geometries are involved (Hawthorn, 1974; Votruba et al., 1975; Schlünder, 1972; Uberoi and Pereira, 1996; Ullah et al., 1992). Correlations have been proposed to describe the local values of the mass-transfer coefficient along the length of the channel (Hwang and Sheu, 1974; Tronconi et al., 1992; VDI-Wärmeatlas, 1991), but Sherwood ($Sh$) numbers are strongly influenced by the form of the equation used. The use of local correlations is still an approximation because they indicate a peripheral average on the contour of the channel cross section. Furthermore, if applied with simplified kinetics, they can lead to inaccuracy. Recent studies and developments of a two-dimensional (2-D) model are presented in articles by Hayes et al. (1995), Groppi et al. (1995) and Leung et al. (1996). Nevertheless, monolith channels are usually square or triangular, so a 3-D model should be used. Using differential balances, Bai and Chwu (1997) recently developed a 3-D model. Detailed simulations were given for the SCR reaction occurring on vanadia/titania-based catalysts, including different channel pitches, temperatures, and $\alpha$-ratios ($NH_3$/NO ratio in feed). However, the model applied by these authors does not consider: (1) the hydrodynamic entrance length, (2) the influence of the oxygen concentration, (3) the direct ammonia oxidation, and (4) the role the real exhaust gas may play compared with synthetic gas conditions. Other differences between their model and our model are in the operating conditions examined. Our 3-D model and kinetic expressions are valid for a wide temperature range (140–475°C) and have been verified for large GHSV changes (14,800 $h^{-1}$–73,900 $h^{-1}$). Furthermore, the flux on the catalytic surface, which is controlled by the effective rate of catalytic reaction between NO and $NH_3$, is derived from the concentration gradients of the reactants at the bulk surface. These expressions have been derived in another study that deals with the global kinetic modeling of the SCR reaction (Roduit et al., 1998). On the other hand, to express the effective rate of the catalytic reaction, Bai and Chwu (1997) relate the concentration gradient at the catalyst surface to the reaction rate by multiplying the Damköhler number ($Da = k_{ER} d_c / 2 D_g$) by a dimensionless rate expression form for NO, and by treating the half channel pitch as the characteristic length. This does not consider the contribution of the direct ammonia oxidation ($NH_3$-ox.) in spite of the fact that the experimental results

**Table 1. Composition of Exhaust Gases for a Performance of 890 kW**

| P (kW) | NO (ppm) | $NO_2$ (ppm) | HC (ppm) | CO (ppm) | $CO_2$ (%) | $O_2$ (%) | $H_2O$ (%) | $SO_2$ (ppm) | $N_2$ + Rest |
|---|---|---|---|---|---|---|---|---|---|
| 890 | 1020 | 115 | 30 | 490 | 7.1 | 10.5 | 4–5 | 30 | balance |

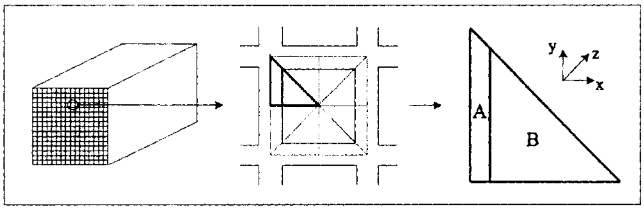


**Figure 1. Honeycomb channel.**

The simulation of the whole monolith reduces to the analysis of a single channel. A—channel wall; B—channel duct.

indicate nonnegligible effects of this side reaction. The results obtained by Bai and Chwu (1997) generally agree with our observations, whereas their values of activation energy and adsorption enthalpy of $NH_3$, calculated for five catalysts, are significantly lower (Bai and Chwu (1997): 16 $kJ \cdot mol^{-1} < E_{ER} < 46$ $kJ \cdot mol^{-1}$, $-47$ $kJ \cdot mol^{-1} < \Delta H_{NH_3} < 0$ $kJ \cdot mol^{-1}$; Roduit et al. (1998): 76 $kJ \cdot mol^{-1} < E_{ER} < 102$ $kJ \cdot mol^{-1}$, $\Delta H_{NH_3} = -139$ $kJ \cdot mol^{-1}$). The 3-D model given here allows calculation of the concentration profiles using finite-element methods and considering the axial ($z$) and cross-sectional ($x$, $y$) conversion progress of both reactants (NO and $NH_3$) in the wall (A) and in the gas phase (B) (Figure 1).

### *Model assumptions*

Due to the low concentrations (ppm-range) of the reacting components of the gaseous mixture and the small amount of evolved heat generated by the reaction, the process can be considered to be almost isothermal (Bai and Chwu, 1997). Furthermore, the experimental conditions are supposed to be identical in all honeycomb channels when assuming a uniform catalyst distribution, an equally distributed inlet flow over the entire cross section of the honeycomb, and an ideal homogeneous premixing of the exhaust gas and reductant mixture. According to these assumptions, the simulation of the physicochemical processes occurring in the whole monolith is reduced to the analysis of a single channel (see Figure 1). In the proposed 3-D model, the occurrence of the selective noncatalytic reduction (SNCR) has been neglected because the temperature is too low to initiate the homogeneous reaction. It is assumed that diffusion obeys Fick's law and that the axial diffusion of the species in the gas phase is negligible when compared to convective contributions (Bahamonde et al., 1996; Bai and Chwu, 1997).

## Concentration Distribution in the Catalyst Wall

### *Generalized mass balance and discretization of the wall domain*

To consider the change in the concentration of the reactant diffusing and reacting inside the catalyst wall (domain A, see Figures 1 and 2), the mass balance for a reactant $S$ reads:

$$D_e \left( \frac{\partial^2 p_S}{\partial x^2} + \frac{\partial^2 p_S}{\partial y^2} \right) = R^* \tag{1}$$

with

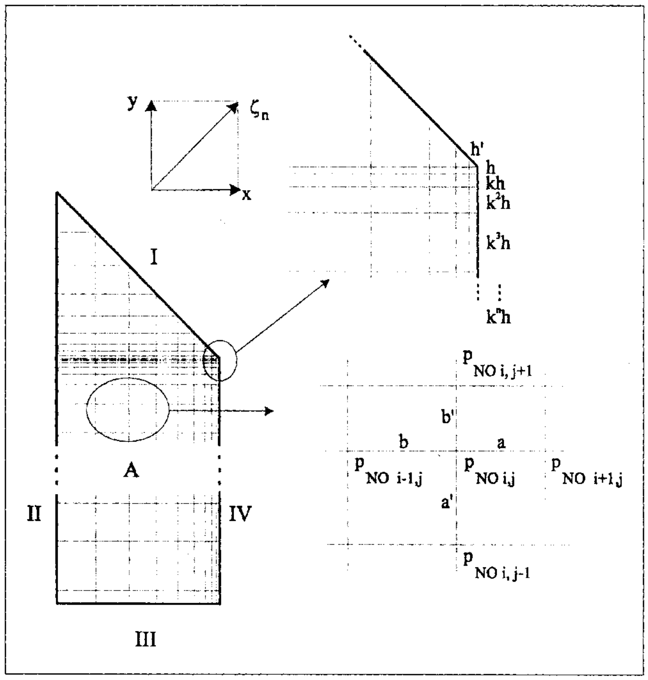


**Figure 2. Domain A.**

The grid-point distribution is chosen with variable step lengths.

$$\frac{\partial p_S}{\partial x} \gg \frac{\partial p_S}{\partial z} \Rightarrow \frac{\partial^2 p_S}{\partial x^2} \gg \frac{\partial^2 p_S}{\partial z^2}$$

and for steady state $(dp_S/dt) = 0$.

Inside the catalyst wall, three boundary conditions (I, II, III; see Figure 2) are derived from the symmetrical properties of one honeycomb channel. The fourth boundary condition (IV; Figure 2) is derived from comparing the fluxes at the interface between the wall (domain A) and the gas phase (domain B). We have:

- Boundaries (I to III): Symmetry axis

$$\frac{\partial p_S}{\partial x} = \frac{\partial p_S}{\partial y} = \frac{\partial p_S}{\partial \zeta_n} = 0. \tag{2,3,4}$$

- Boundary (IV): Considering the left and right sides of the interface, we can write

$$n_x|_{\text{bulk side}} = n_x|_{\text{gas side}} \Leftrightarrow D_e \left.\frac{\partial p_S}{\partial x}\right|_{\text{bulk side}} = D_g \left.\frac{\partial p_S}{\partial x}\right|_{\text{gas side}}. \tag{5}$$

The concentration distribution inside the catalyst wall (domain A) can be calculated using the boundary conditions expressed by Eqs. 2 to 5 in Eq. 1. This allows us to write for NO:

$$D_e \left( \frac{\partial^2 p_{NO}}{\partial x^2} + \frac{\partial^2 p_{NO}}{\partial y^2} \right) = R_{NO}. \tag{6}$$

The numerical treatment is described in Appendix A. Figure 3 shows the concentrations of NO calculated for an arbitrary constant value of NO (1,000 ppm) at the wall surface.

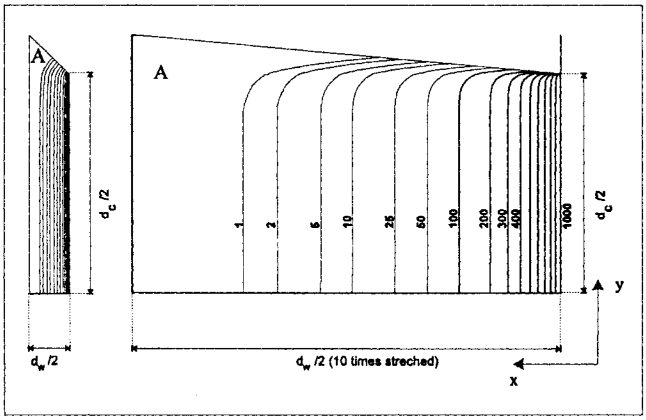


**Figure 3. Domain A: concentration distribution of NO (on the curves in ppm) inside the catalyst wall at $T = 300°C$.**

It was calculated by assuming the concentration of 1,000 ppm NO at the surface. The concentration profiles are represented for an eighth of channel.

The strong internal gradients indicate that the reaction is confined to a very thin layer near the surface of the catalyst wall. It also indicates that the partial pressure gradients $\partial p_S/\partial y$ amount to zero in most of the reaction zone within the wall, except at the channel corners. It follows that the gradient in the $y$-direction can be neglected if compared to the one in the $x$-direction:

$$\frac{\partial p_S}{\partial x} \gg \frac{\partial p_S}{\partial y} \Rightarrow \frac{\partial^2 p_S}{\partial x^2} \gg \frac{\partial^2 p_S}{\partial y^2}. \tag{7}$$

Equation 6, which describes the partial pressure profile for NO inside the wall, can consequently be well approximated by Eq. 8:

$$D_e \frac{\partial^2 p_S}{\partial x^2} \cong R^*, \tag{8}$$

which ensures good accuracy, in spite of the fact that the diffusion along the $y$-direction is not considered. The slight inaccuracy of this assumption is entirely dependent on the channel opening.

## Concentration Distributions in the Gas Phase

### *Hydrodynamic entrance lengths and laminar velocity*

The velocity distribution in a fluid flowing through the honeycomb channel evolves from the initial profile at the inlet to a fully developed profile at a certain location downstream. For engineering calculations, the axial distance required for the center-line velocity to achieve 99% of the fully established velocity is defined as the hydrodynamic entrance length. Many authors (Langhaar, 1942; Han, 1960; Van Dyke, 1970; Schlichting, 1979) have tried to determine the exact nature of the flow development in the entrance region. The usual boundary layer analysis, which assumes a small region close to the duct wall in which shearing stress is large, leads to the following conclusions (Han, 1960): (i) $(\partial^2 u/\partial z^2) \ll (\partial^2 u/\partial x^2, \partial^2 u/\partial y^2)$; (ii) $(u_x, u_y) \ll u_z$; and (iii) $\partial p/\partial z = f(z)$ only. Even for laminar conditions, however, the velocity problem of the entrance region does not yield an exact solution. The difficulties in the analysis can be traced to the nonlinearity of the inertia term that appears in the equation of motion; conditions (i), (ii) and (iii) lead to the following, reduced form of this equation:

$$u_z \frac{\partial u_z}{\partial z} = \upsilon \left( \frac{\partial^2 u_z}{\partial x^2} + \frac{\partial^2 u_z}{\partial y^2} \right) - \frac{1}{\rho} \frac{\partial p}{\partial z} \tag{9}$$

Applying Langhaar's method (1942), which consists of the linearization of Eq. 9, we can replace the lefthand side convective terms by $(\upsilon \beta^2 u_z)$. The resulting equation is:

$$\frac{1}{\mu} \frac{\partial p}{\partial z} + \beta^2 u_z = \left( \frac{\partial^2 u_z}{\partial x^2} + \frac{\partial^2 u_z}{\partial y^2} \right) \tag{10}$$

where $\beta$ is a function of $z$ only. Solution of this equation assumes the form of a fully developed velocity profile when $\beta = 0$, and a uniform velocity profile at $\beta = \infty$, thus providing a smooth transition. Considering the transition profile, the problem has been solved using numerical computations by Han (1960) for rectangular ducts with channel edges $a = d_{c1}$ and $b = d_{c2}$. Han carried out the calculations for six aspect ratios $\gamma = a/b$, and 36 $\beta$ values were selected for each by evaluating the velocity profile. Integrating over the section of the duct, he obtained the following single-summation expressions (Eq. 11–13):

$$u(x,y) = \bar{u} \frac{F_1}{F_2}, \tag{11}$$

where

$$F_1 = \frac{1}{\beta^2 a^2} \left( \frac{\cosh \beta x}{\cosh \beta a} - 1 \right) + \sum_{n=1,3,5\ldots} \frac{16(-1)^{(n-1)/2} \cos(n\pi x/2a)}{\pi^3 n \left[ n^2 + (2\beta a/\pi)^2 \right]} \times \frac{\cosh\left\{ \frac{\pi}{2\gamma} \left[ n^2 + (2\beta a/\pi)^2 \right]^{1/2} \frac{y}{b} \right\}}{\cosh\left\{ \frac{\pi}{2\gamma} \left[ n^2 + (2\beta a/\pi^2) \right]^{1/2} \right\}} \tag{12}$$

$$F_2 = \frac{1}{\beta^2 a^2} \left( \frac{\text{tank}\, \beta a}{\beta a} - 1 \right) + \sum_{n=1,3,5\ldots} \frac{32}{\pi^4 n^2 \left[ n^2 + (2\beta a/\pi)^2 \right]} \times \frac{\tanh\left\{ \frac{\pi}{2\gamma} \left[ n^2 + (2\beta a/\pi)^2 \right]^{1/2} \right\}}{\frac{\pi}{2\gamma} \left[ n^2 + (2\beta a/\pi)^2 \right]^{1/2}}. \tag{13}$$

The $\beta a$ values as a function of the $z$-coordinates $(z/D_e Re)$ for the given aspect ratio $\gamma = a/b = 1$ (square ducts) are presented in Table 2. The hydrodynamic entrance length is attained when $\beta a = 0.59$ (Han, 1960). The magnitude of the

Table 2. Determination of the Velocity Profiles Inside a Channel*

| $\beta a$ | $z/D_e Re$ | $\beta a$ | $z/D_e Re$ | $\beta a$ | $z/D_e Re$ |
|---|---|---|---|---|---|
| $\infty$ | 0 | 2.00 | 0.02642 | 0.50 | 0.08266 |
| 20 | 0.00018 | 1.80 | 0.03003 | 0.45 | 0.08712 |
| 10 | 0.00098 | 1.60 | 0.03428 | 0.40 | 0.09209 |
| 8 | 0.00172 | 1.40 | 0.03934 | 0.375 | 0.09563 |
| 6 | 0.00348 | 1.20 | 0.04544 | 0.350 | 0.09851 |
| 5 | 0.00532 | 1.00 | 0.05297 | 0.325 | 0.10084 |
| 4 | 0.00857 | 0.90 | 0.05737 | 0.300 | 0.10333 |
| 3.50 | 0.01110 | 0.80 | 0.06236 | 0.275 | 0.10646 |
| 3.00 | 0.01459 | 0.70 | 0.06812 | 0.250 | 0.11987 |
| 2.75 | 0.01681 | 0.65 | 0.07132 | 0.225 | 0.13020 |
| 2.50 | 0.01946 | 0.60 | 0.07480 | 0.200 | 0.17977 |
| 2.25 | 0.02262 | 0.55 | 0.07854 | | |

*For an aspect ratio $\gamma = a/b = 1$ (square ducts), the hydrodynamic entrance length is attained when $\beta a \leq 0.59$.

velocity at any point $(x, y, z)$ inside the channel can be determined by evaluating Eqs. 11–13 with the aid of the $\beta a$-values of Table 2. The development of the velocity distribution can be clearly portrayed by a sequence of velocity profiles at various axial positions along the channel (Figure 4). The profiles in the immediate neighborhood of the entrance ($\beta a > 5$) have a distinct flat portion in the region away from the channel wall. The velocity distribution profile can be regarded as unchanged when $\beta a < 0.59$. These velocity profiles, which describe the fluid dynamics of the system, will be used to calculate the concentration distribution of NO and $NH_3$ over the entire cross section and along the length of the channel.

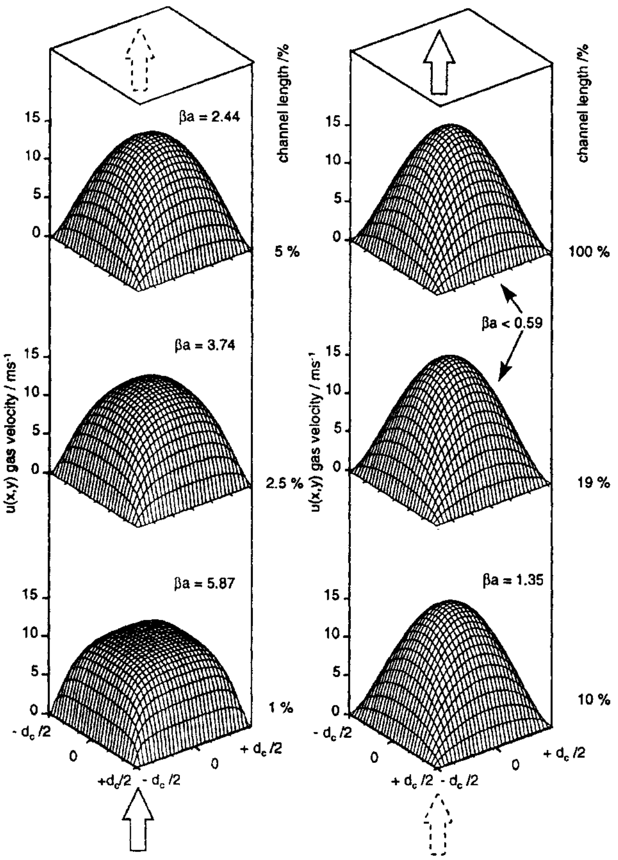


**Figure 4. Developing laminar velocity profiles in a channel.**

The calculations were performed for $T = 400°C$ and $Re = 408$ ($F = 1{,}500\ m^3/h$, GHSV $= 44{,}343\ h^{-1}$). The laminar velocity profile is fully developed (hydrodynamic entrance length) after ca. 19% of the length of the channel when $\beta a < 0.59$.

### *Generalized mass balance and discretization of the 3-D domain*

The geometry of the catalytic support is made of square ducts. Using the model assumptions and considering the hydrodynamic entrance length, a 3-D steady-state mass transfer model gives for a reactant $S$:

$$u_x(x,y,z)\frac{\partial p_S}{\partial x} + u_y(x,y,z)\frac{\partial p_S}{\partial y} + u_z(x,y,z)\frac{\partial p_S}{\partial z} = D_g\left(\frac{\partial^2 p_S}{\partial x^2} + \frac{\partial^2 p_S}{\partial y^2}\right). \quad (14)$$

Since the entrance length is much shorter than the length of a channel (see Figure 4) and $u_z \gg u_x (u_z \gg u_y)$, we can consider only one convection term for a reactant $S$, that is, $u_z(\partial p_S/\partial z)$ in Eq. 14, that is still accurate enough despite the fact that $u_x \neq u_y \neq 0$ and

$$\frac{\partial p_S}{\partial x} \gg \frac{\partial p_S}{\partial z}\left(\frac{\partial p_S}{\partial y} \gg \frac{\partial p_S}{\partial z}\right).$$

However, if the convective terms in the $x$-$y$ directions are discarded, we have to confirm that this simplification holds true when we compare both convection and diffusion in the $x$-$y$ directions, that is, we have to show that the following relationships are correct before the velocity profile is fully developed:

$$u_x\frac{\partial p_S}{\partial x} \ll D_g\frac{\partial^2 p_S}{\partial x^2} \text{ or } \frac{u_x(d_c/2)}{D_g} \ll 1, \quad (15)$$

where $d_c/2$ is the characteristic length for mass transfer in direction $x$. In order to bring out the essential features of Eq. 14, an approximation of $u_x$ is required. From the equation of continuity, $u_x$ (central) can be estimated as it follows:

$$\frac{\partial u_x}{\partial x} \approx -\frac{1}{2}\frac{\partial u_z}{\partial z} \quad \text{as} \quad \frac{\partial u_x}{\partial x} \approx \frac{\partial u_y}{\partial y} \Rightarrow \frac{\Delta u_x}{(d_c/2)} \approx \frac{1}{2}\frac{\Delta u_z}{\Delta z}$$
$$\Rightarrow u_x \approx \frac{(d_c/2)}{2\Delta z}\Delta u_z, \quad (16)$$

where $\Delta z$ is the entrance length and $\Delta u_z$ the increase in velocity (central). For example, at $T = 400°C$ and $Re = 408$, the rough estimation of $u_x(d_c/2)/D_g$ amounts to ca. 0.7. This means that the elimination of the convective terms in the $x$-$y$ direction is incomplete at the entrance of the channel only and, after a few percent of length, becomes increasingly legitimate when $u_x$ ($u_y$) drops asymptotically to zero and the fully developed profile tends to be reached. Once the hydrodynamic entrance length is reached, we have $u_z = u_z(x, y)$, and therefore:

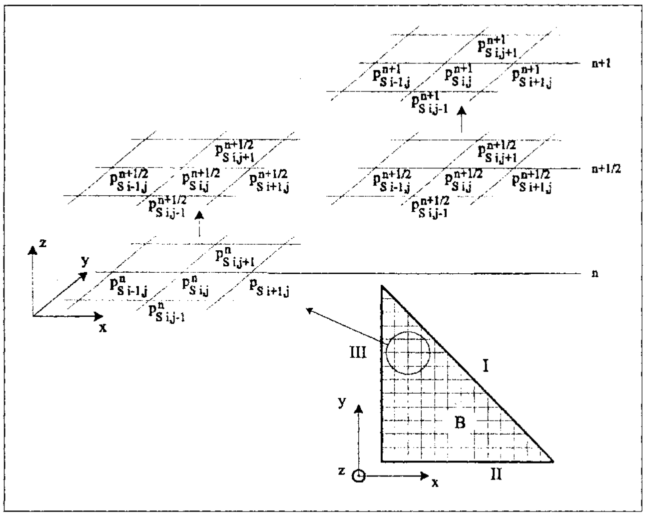


**Figure 5. Applied 3-D mesh (ADI algorithm) for a given reactant $S$ (domain B).**

The applied 3-D mesh can be divided into a series of $N$ mesh planes, each having $I \times J$ elements.

$$\left\{\begin{aligned} \frac{\partial p_{\mathrm{NO}}}{\partial z} &= \frac{D_g}{u_z(x,y)}\left(\frac{\partial^2 p_{\mathrm{NO}}}{\partial x^2}+\frac{\partial^2 p_{\mathrm{NO}}}{\partial y^2}\right)\\ \frac{\partial p_{\mathrm{NH_3}}}{\partial z} &= \frac{D_g}{u_z(x,y)}\left(\frac{\partial^2 p_{\mathrm{NH_3}}}{\partial x^2}+\frac{\partial^2 p_{\mathrm{NH_3}}}{\partial y^2}\right). \end{aligned}\right. \tag{17a,b}$$

In the gas phase, boundary conditions I and II (Figure 5) are based on the symmetrical properties of one honeycomb channel (Eqs. 3–4), whereas boundary III (Figure 5) is derived from a comparison of the fluxes (Eq. 5).

The solution of the preceding system of partial differential equations (Eqs. 17a, 17b) consists of solving parabolic equations in 3-D space. An explicit solution can be obtained by substituting finite-difference approximations for the first and second derivates of $p_{\mathrm{NO}}$ and $p_{\mathrm{NH_3}}$. A method known as alternating-direction implicit (ADI), which is one of a group of techniques called *splitting methods*, offers an efficient way of solving these kinds of equation (Scraton, 1987; Chapra and Canale, 1988; Gerald and Wheatley, 1989). The ADI scheme provides a means of solving parabolic equations in 3-D space using tridiagonal matrices. Figure 5 illustrates the discretization of the governing partial differential equations (Eqs. 17a and 17b) by describing the physical and chemical processes occurring inside a honeycomb channel. Consideration of the entrance length effects, complex kinetics, and symmetries in the numerical treatment makes the mathematical approach more demanding, but much more precise. The use of the channel's symmetrical properties (domain B, boundaries I and II, Figure 5) decreases, by order of magnitude, the calculation time. This method allows the calculation of the concentrations of both reactants NO and $NH_3$ at each location $z$ for every $x$, $y$ grid points.

### *Calculated vs. experimental data*

The mean partial pressures of NO and $NH_3$ at the inlet and at the outlet of the honeycomb were obtained using the following expressions:

$$\bar{p}_{\mathrm{in}} = \bar{p}_{z=0} = \frac{\int_S u_0 p_0 \, dS}{\int_S u_0 \, dS} \tag{18}$$

$$\bar{p}_{\mathrm{out}} = \bar{p}_{z=L} = \frac{\int_S u_L p_L \, dS}{\int_S u_L \, dS}. \tag{19}$$

The results of the simulation of the SCR reaction in real exhaust-gas conditions were compared with the experimental data obtained by Bettoni (1997). Several experiments were performed in which the temperature and flow rate were varied. The NO removal (Figure 6A, $T = 200°C$), as well as the $NH_3$ slip (Figure 6B, $T = 400°C$), are presented with their corresponding simulated data (solid curves) for flow rates between 500 and 2,000 $m^3/h$. Similar behavior and fittings for both NO removal and $NH_3$ slip have been obtained at 250, 300, 350 and 430°C.

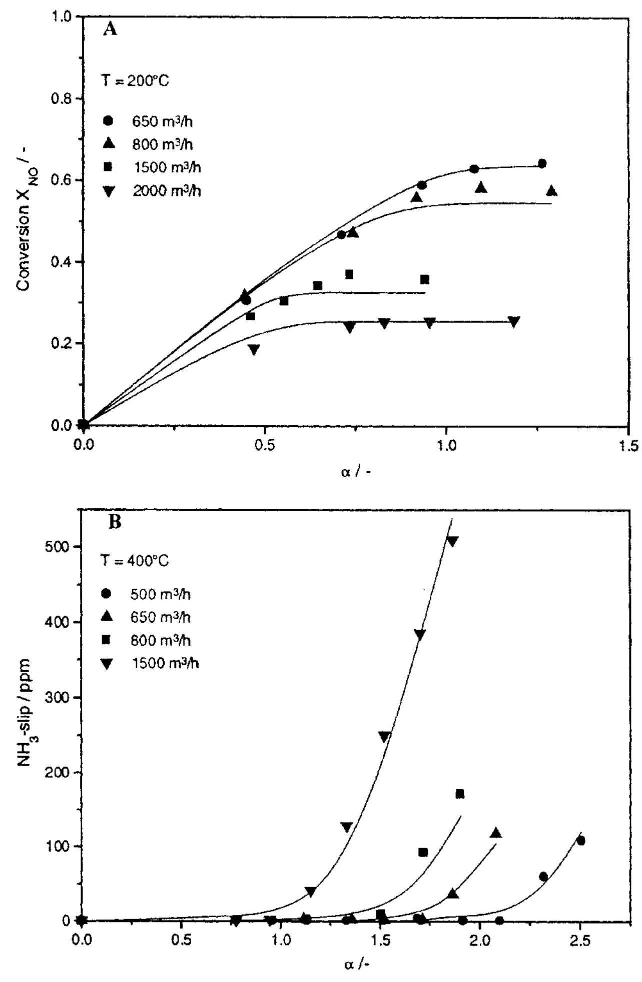


**Figure 6. Conversion of NO [($T$ = 200°C (A)] and $NH_3$ slip [($T$ = 400°C (B)] for different flow rates.**

The solid curves represent the simulated values. Concentrations of $NO_{in}$ vary between 1020 and 1150 ppm.

**Table 3. Calculated Kinetic Constants***

| | $A_{ER}^{a}$ ($m^3 \cdot kg^{-1} \cdot s^{-1}$) | $E_{ER}^{a}$ ($kJ \cdot mol^{-1}$) |
|---|---|---|
| Synthetic gas | $1.20 \times 10^{9}$ | 101.9 |
| Real gas | $9.65 \times 10^{7}$ | 85.3 |
| | $K_{oO_2}/Pa^{-1}$ | $\Delta H_{O_2}/kJ \cdot mol^{-1}$ |
| Synthetic + real gas | $6.01 \times 10^{9}$ | −47.4 |
| | $A_{NH_3-ox.}$ ($Pa \cdot m^3 \cdot kg^{-1} \cdot s^{-1}$) | $E_{NH_3-ox.}$ ($kJ \cdot mol^{-1}$) |
| Synthetic + real gas | $7.22 \times 10^{6}$ | 76.4 |
| | $K_{oNH_3}$ ($Pa^{-1}$) | $\Delta H_{NH_3}$ ($kJ \cdot mol^{-1}$) |
| Synthetic + real gas | $3.78 \times 10^{-12}$ | −139.2 |

*Kinetic constants have been calculated from microreactor experiments (synthetic gas). The 3-D model for the honeycomb (real gas) has been compared with the data on a predictive basis. Only the $k_{ER}$ constant has been refitted for real exhaust gas conditions where higher catalytic activity could be observed.

### *Role of real exhaust gas and effective diffusivities*

Kinetics of the SCR of NO with $NH_3$ and the $NH_3$ oxidation, applied later for the *De*$NO_x$ and $NH_3$ slip calculations on a large honeycomb scale, have been determined using microreactor experiments (Roduit et al., 1998). Note, however, that the reported kinetic constants were obtained under synthetic gas conditions, which differed from the industrial ones. Nevertheless, the match between the computational and experimental results were predictable (Figure 6). Sensitivity analysis, performed with Matlab V (The MATHWORKS, Inc.), has demonstrated that only one constant, $k_{ER}$, which expresses with $k_{NH_3\text{-ox.}}$ the main (*ER* = Eley Rideal) and side reaction ($NH_3$-ox.), that is, the selectivity of the SCR reaction, is "sensitive" to gas composition. This constant was therefore refitted for a more accurate representation of the NO removal process and $NH_3$ slip under real exhaust-gas conditions. It could be observed that under real flue-gas conditions one has to reckon with higher activity ($k_{ER}$ higher). The calculated constants are listed in Table 3. Effective diffusivities of the reactants inside the catalyst have been estimated experimentally by using the same method as previously used by Beeckmann (1991). The technique of measurement involves the gas stream passing inside and outside a particular monolith channel and measuring the net flux across its walls. The values for NO at six different temperatures are listed in Table 4.

### *NO and $NH_3$ concentration vs. channel length*

The 3-D model programmed with the software Matlab V (The MATHWORKS, Inc.) enabled calculations of the velocity profile, the concentration distribution, the concentration gradients, and the reaction progress at every ($x$, $y$, $z$) point of the computed 3-D mesh for a given temperature, flow rate, and $\alpha$-ratio (Figure 7). Figure 8 shows the concentration distribution profiles of NO and $NH_3$ for 5-, 10-, 50-, and 100% of the length of a channel for an inlet $\alpha$-ratio = 1. As these figures for the main part of the channel show, the concentration at the wall surface is significantly lower than the mean concentration and the concentration in the center of the channel. The concentration in the center still remains almost constant during the first 10% of the whole channel length. At 10% ($\alpha = 0.5$, Figure 7A, middle) and 50% ($\alpha = 1$, Figure 7B, middle) of the channel length, respectively, the $NH_3$ concentration at the wall surface drops to nearly zero for $\alpha$ ratios $\leq 1$. This explains the linear augmentation of the NO conversion with an increasing supply of $NH_3$ and the absence of the ammonia slip for these $\alpha$-values and the operating conditions considered. The $NH_3$ concentration decrease is faster (Figures 7 and 8) than the NO removal because of the direct $NH_3$ side oxidation, the relevance of which is, among other things, dependent on the $\alpha$-ratio (see Figures 7A, 7B, and 7C, bottom). For 50 and 100% of the channel length, only minor changes of the NO concentration profile are observable, as shown in Figures 7 and 8. The $NH_3$ concentration becomes negligible at the catalyst surface, the *De*$NO_x$ reaction comes to a standstill, and the NO concentration profile subsides over the entire cross section. These observations are in line with the ones of Bai and Chwu (1997) for SCR-*De*$NO_x$.

**Table 4. Measurements of Effective Diffusivities of NO at Different Temperatures**

| $T$ | $D_{eNO}/m^2 \cdot s^{-1}$ |
|---|---|
| 200 | $4.47 \times 10^{-7}$ |
| 250 | $5.57 \times 10^{-7}$ |
| 300 | $6.59 \times 10^{-7}$ |
| 350 | $7.52 \times 10^{-7}$ |
| 400 | $8.39 \times 10^{-7}$ |
| 450 | $9.20 \times 10^{-7}$ |

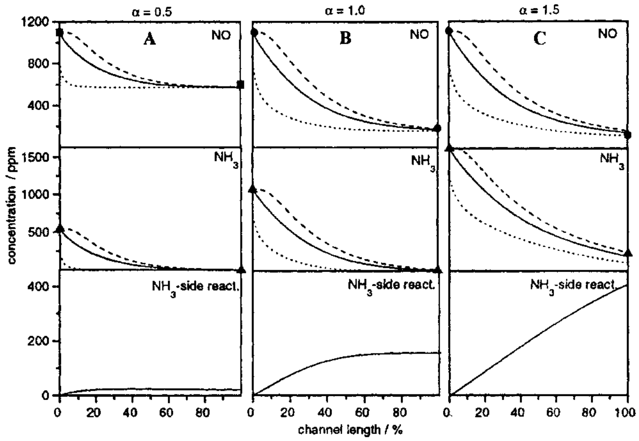


**Figure 7. Concentrations of NO (top) and $NH_3$ (middle) along the length of the channel for different $\alpha$-ratios [(A) $\alpha = 0.5$; (B) $\alpha = 1.0$; (C) $\alpha = 1.5$)].**

The dashed, solid and dotted curves represent the concentration in the center of the channel, the mean concentration, and the concentration at the wall, respectively. Oxidation of $NH_3$ occurring through the $NH_3$ side ($NH_3$-ox.) is presented in the bottom figures. ●, ▲ = experiment data. $T = 400°C$; $NO_{in} = 1,100$ ppm; $F = 1,500$ $m^3/h$ ($Re = 408$, GHSV = 44,343 $h^{-1}$).

### *Mass-transfer resistance*

The external mass transfer is high at the inlet of the honeycomb, and its effect levels off downstream. At high temperatures the reaction rate is much more accelerated compared

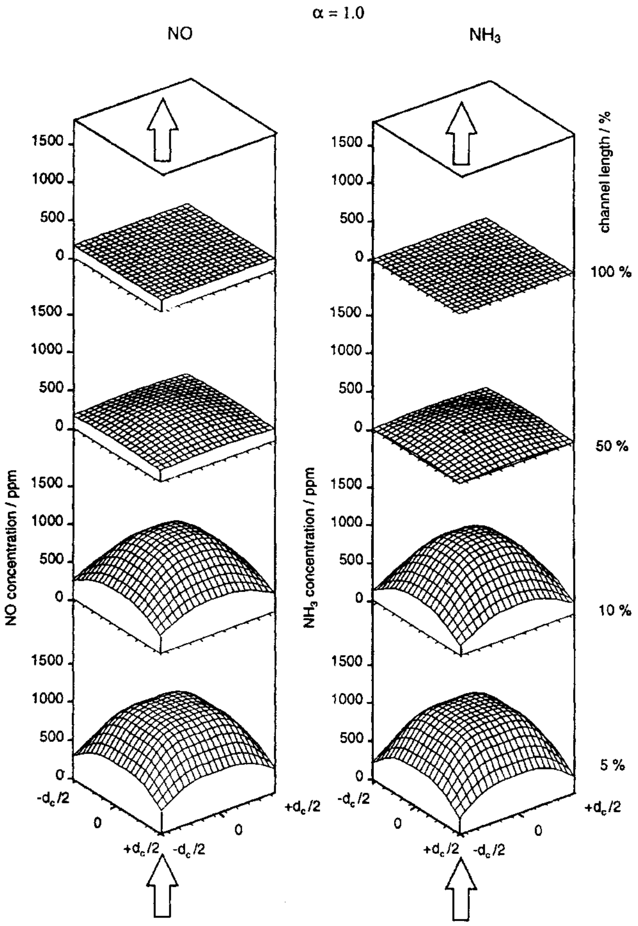


**Figure 8. Radial and axial distribution profile of NO and $NH_3$ along the length of the channel.**

NO (left), $NH_3$ (right). The direction of the gas flow is shown by the arrow. $\alpha = 1$; $NO_{in} = 1{,}000$ ppm; $T = 400°C$; $F = 1{,}500$ $m^3/h$ ($Re = 408$, GHSV $= 44{,}343$ $h^{-1}$).

to the rate of the mass transfer, and the concentration at the wall surface continuously decreases until the mass transfer becomes the rate-limiting step slowing down the $De$NO$_x$ process. The higher the reaction rate and the lower the flow rate are, the shorter the distance is between the channel entrance and the axial position at which mass transfer becomes rate limiting.

Using the 3-D model one can calculate the local and mean $Sh$-numbers that describe the local and mean values of the mass-transfer coefficients along the length of the channel for any experimental conditions (Figures 9A and 9B). Let us consider the relationships for the mean partial pressure in the channel (Eq. 20), the mean partial pressure at the wall surface (Eq. 21), and the mean partial pressure gradient at the wall surface on the gas-phase side (Eq. 22):

$$\bar{p}_z = \frac{\int_S u_z p_z \, dS}{\int_S u_z \, dS} \qquad (0 < z < L) \tag{20}$$

$$\bar{p}_{z,\text{wall}} = \frac{1}{L_c} \int_0^{L_c} p_z \, dl \tag{21}$$

$$\left.\frac{d\bar{p}}{dx}\right|_{z,\text{gas side}} = \frac{1}{L_c} \int_0^{L_c} \left.\frac{dp}{dx}\right|_{z,\text{gas side}} dl. \tag{22}$$

The mass-transfer coefficients $k_m$ (local Eq. 24a, mean Eq. 25a) and their corresponding $Sh$ numbers (local Eq. 24b, mean Eq. 25b) can be computed by means of Eq. 23:

$$D_g \left.\frac{d\bar{p}}{dx}\right|_{z,\text{ gas side}} = k_{m,\text{ local},\, z}\left(\bar{p}_z - \bar{p}_{z,\text{ wall}}\right) \qquad (0 < z < L) \tag{23}$$

$$\Rightarrow k_{m,\text{local},z} = \frac{D_g \left.\frac{d\bar{p}}{dx}\right|_{z,\text{gas side}}}{\bar{p}_z - \bar{p}_{z,\text{wall}}} \Rightarrow Sh(z) = Sh_{\text{local},z} = \frac{k_{m,\text{local},z}\, d_c}{D_g} \qquad (0 < z < L) \quad \text{(24a-b)}$$

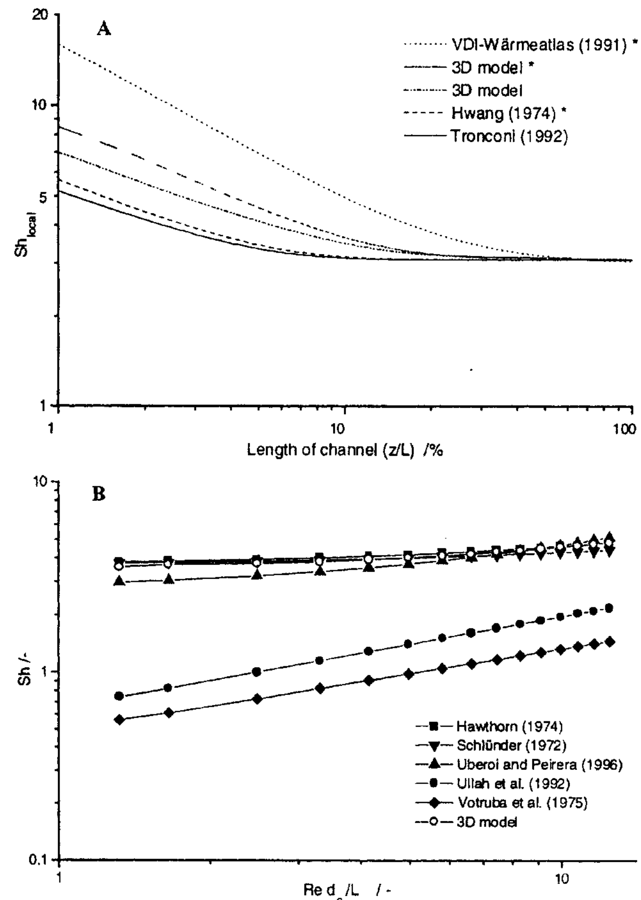


**Figure 9. $Sh$ numbers [(A), local; (B), mean] as predicted by various correlations and the 3-D model as a function of (A) the channel length; and (B) $Re\ d_c/L$.**

Calculations were performed for $T = 400°C$

$$\Rightarrow k_m = \frac{1}{L}\int_0^L k_{m,\mathrm{local},z}\,dz \Rightarrow Sh = \frac{k_m d_c}{D_g}. \quad \text{(25a-b)}$$

The results of the calculations are presented in Figures 9A and 9B. The simplifying assumption of fully developed laminar flow affects the $Sh_{\mathrm{local}}$ profile (Figure 9A). Since for long channels the effects associated with the development of the velocity profile are of the same magnitude as those of the experimental errors, models that do not account for the hydrodynamic entrance effects can be used for long channels. These models, however, can lead to inaccuracies when the channel is shorter (e.g., in the case of honeycomb segments in series), since ignoring the developing boundary layer results in underestimating the mass transfer, and therefore in overestimating the NO and $NH_3$ outlet concentrations. The last effect depends, of course, on the initial $\alpha$ ratio.

### *$NH_3$ concentration and NO conversion for 10 ppm $NH_3$ slip as a function of temperature and gas flow rate*

For a given flow rate and temperature, SCR-*De*$NO_x$ rates are maximal when the relative ammonia coverage $\Theta_{NH_3}$ over the catalyst reaches its highest value, which is about 1. If the relative ammonia coverage is smaller than 1, it indicates that not all available reaction sites are occupied, which leads to a decrease of the reaction rate. A possible way to augment the number of reactive sites is to increase the $\alpha$ ratio at the entrance of the honeycomb, but too large a reductant distribution would contribute to an excessive $NH_3$ slip at the outlet of the SCR reactor. It follows that for a given flow rate, temperature, and honeycomb design, such an $\alpha$ ratio must be regulated in order to achieve high $D_e NO_x$ efficiency and low $NH_3$ slip. In this sense, the 3-D model would be an efficient solution for fine-tuning the $\alpha$-ratio for a given temperature, gas flow rate, and acceptable $NH_3$ slip (see Figures 10A and 10B).

The predicted concentrations for $NH_3$ at the entrance of the honeycomb and their corresponding isoconversion lines for NO have been calculated with the 3-D model using Eqs. 18 and 19. The most suitable inlet $NH_3$ concentrations have been calculated for each flow rate (1,000 $m^3/h < F <$ 1,600 $m^3/h$) and temperature (200°C $< T <$ 400°C) by minimizing the squared difference between the arbitrarily taken maximal $NH_3$ slip, such as, for example, 10 ppm ($\bar{p}_{NH_3\,\mathrm{out,standard}}$), and the computed $NH_3$ slip ($\bar{p}_{NH_3\mathrm{out}}$). The optimization has been performed by setting

$$\left(\bar{p}_{NH_3\mathrm{out}} - \bar{p}_{NH_3\mathrm{out,standard}}\right)^2 = 0 \qquad (26)$$

and adjusting $\bar{p}_{NH_3\mathrm{in}}$, which is the required partial pressure of ammonia at the inlet of the honeycomb.

An example explaining the use of Figures 10A and 10B is: Let us assume that the concentration of NO in the exhaust gas is 1,000 ppm for a performance of 900 kW, and that the corresponding gas temperature is 370°C with a gas flow rate amounting to 1,300 $m^3/h$. By applying these operating conditions in Figure 10A, it emerges that for the maximal, arbitrarily taken $NH_3$ slip (10 ppm), the required inlet $NH_3$ concentration is 1,080 ppm. The ensuing NO conversion reaches 90%, and can be read in Figure 10B. Consideration of different NO concentrations to generalize the calculations in Figure 10 would result in a graphical representation that is far too complicated for the scope of the present article. For practical application and control of the appropriate $NH_3$ concentration at the entrance of the honeycomb, however, it is worth calculating several figures similar to Figure 10 for different NO inlet concentrations (e.g., between 900 and 1,300 ppm). This is the goal of further studies.

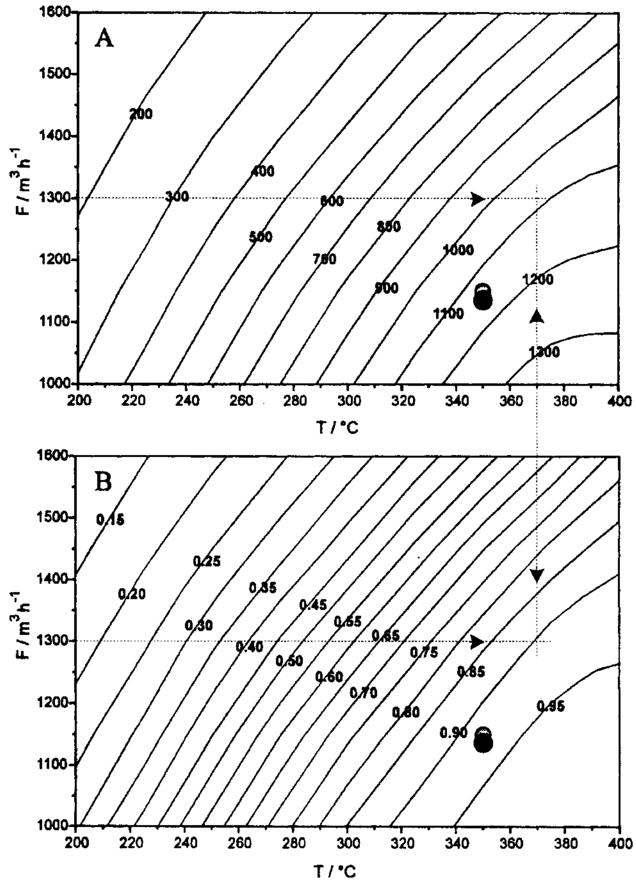


**Figure 10. Inlet $NH_3$ concentration in (A) ppm and corresponding (B) NO conversion for achieving 10-ppm $NH_3$ slip as a function of the temperature and flow rate.**

Calculations have been carried out for a flue gas containing 1,000 ppm NO. It describes the operating conditions for 90% NO-removal at 350°C according to manufacturer (Hüls GmbH, Germany) data. Dashed lines are explained in the example of the text.

### *$NH_3$ concentration and $NH_3$ slip for 90% NO conversion as a function of temperature and gas flow rate*

The results of calculations presented in Figures 11A and 11B allow us to predict the required $NH_3$ concentration in the reactant mixture and ensuing $NH_3$ slip for 90% NO conversion as a function of temperature and gas flow rate. The optimization was performed by setting:

$$\left[\bar{p}_{\mathrm{NOout}} - \bar{p}_{\mathrm{NOin}}\left(1 - X_{\mathrm{NOstandard}}\right)\right]^2 = 0 \qquad (27)$$

and adjusting $\bar{p}_{NH_3\mathrm{in}}$ where the standard conversion $X_{\mathrm{NOstandard}}$ has been arbitrarily fixed at 90%.

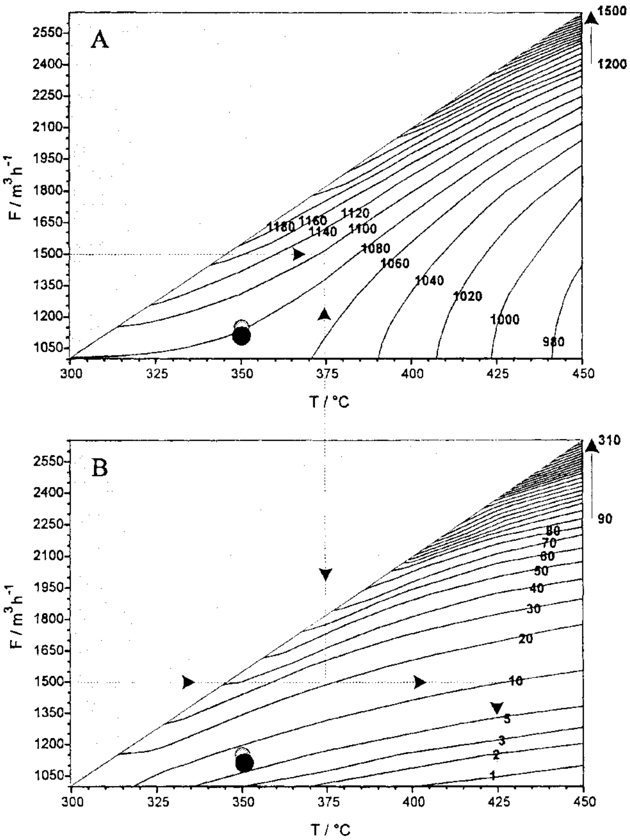


**Figure 11. Inlet $NH_3$ concentration in (A) ppm and corresponding $NH_3$ slip in (B) ppm for achieving 90% NO conversion as a function of the temperature and flow rate.**

The surface in gray represents the domain where 90% $NO_x$ conversion is not possible with the actual honeycomb configuration. Calculations have been carried out for a flue gas containing 1,000 ppm NO. It describes the operating conditions for 90% NO-removal at 350°C according to manufacturer (Hüls GmbH, Germany) data. Dashed lines are explained in the example of the text.

An example of the application of the relationships shown in Figures 11A and 11B to a flue gas containing 1,000 ppm NO is: For a gas flow rate of 1,500 m$^3$/h and a temperature of 375°C, the concentration of $NH_3$ in the inlet stream should amount to approximately 1,100 ppm in order to achieve the 90% NO conversion (Figures 11A). For these conditions, the obtained $NH_3$ slip is 20 ppm (Figure 11B). In order to get the $NH_3$ slip equal 10 ppm, it is necessary to increase the temperature to ca. 425°C.

The manufacturer (Hüls GmbH, Germany) has set the utilized catalytic pollution equipment to achieve 90% NO removal efficiency for a total gas flow rate of 500 Nm$^3$/h (1,141 m$^3$/h at a temperature of 350°C). The position of the operating point is drawn in Figures 10 and 11, and is in good agreement with our calculations.

## Conclusion

Based on finite-element methods and developing a 3-D model, a novel scheme for simulating the SCR of NO with $NH_3$ has been presented. The application of the 3-D model leading to the relationships presented in Figures 10 and 11 is an effective tool for designing the most suitable $NH_3$/NO feed ratio to comply with the NO emission requirements. The application of the relationships presented allows us to choose the proper operating conditions for a given flow rate and temperature of the inlet gases, ones that are interrelated with the performance of the diesel engine. This possible extension of the operating conditions of the honeycomb makes its application more flexible and practice-oriented.

Due to a detailed consideration of the physicochemical processes occurring in the catalytic honeycomb and the small number of assumptions made, the 3-D model provides valuable insight into the performance of the SCR unit. Model agreement is considered especially strong because of the comparison of the manufacturer's set point and the experimental one to the calculated data. It may be used efficiently to characterize the monolith reactor's behavior, to predict the effect of the design parameters, and adjust the appropriate $NH_3$ insertion into the system to achieve minimal $NH_3$ slip and maximal NO abatement.

The appropriate dosage of ammonia is not equimolar with the amount of NO to be removed due to the direct $NH_3$ oxidation ($NH_3$-ox.), whose relevance to and influence on the NO removal and $NH_3$ slip depend on (1) catalyst; (2) $\alpha$-ratio (Figures 7A, 7B, and 7C: bottom, and Figure 8); (3) temperature, length of the honeycomb, and gas flow rate (GHSV) (Figure 6); (4) possible imperfect mixing of $NH_3$ with NO (see ammonia injection system).

Ignoring points (1)–(4) is a common cause of improper application of the $\alpha$-ratio, which can give rise to an undesirable $NH_3$ slip. The ammonia emission limits are usually more strict than those of NO. This drawback may be overcome, however, by applying the relationships of Figure 10. Incorporating an appropriate safety margin due to experimental fluctuations and calculating similar relationships as presented in Figure 10 for different NO concentrations in the flue gas, the applied method should invariably meet the required NO and $NH_3$ emission standards set by the legislation.

## Acknowledgments

Financial support of this work by the Nationaler Energie-Forschungs-Fond (NEFF-Project 569) is gratefully acknowledged. Thanks are due to Katalysatorwerke Hüls GmbH, Germany, for providing the catalyst.

## Notation

$D_g$ = diffusion coefficient in the gas phase
$d_c$ = channel diameter
$d_w$ = wall thickness
$E$ = activation energy
$\Delta H$ = adsorption enthalpy
$i$ = $i$th node of the mesh plane
$j$ = $j$th node of the mesh plane
$n$ = $n$th mesh plane
$k_{ER}$ = reaction rate constant for the Eley-Rideal-type reaction between adsorbed ammonia and gaseous NO
$K_0, A$ = preexponential factors of Van't Hoff and Arrhenius equations
$L$ = channel length, m
$L_c$ = contour of the channel cross section (4 $d_c$)
$n_{x,(y,z)}$ = mass transfer in the $x$-, ($y$-, or $z$-) direction
$R^*, R$ = reaction-rate term

$Re$ = Reynolds number

$S$ = channel cross section ($d_c \times d_c$)

$u_{x,(y,z)}$ = gas velocity in the $x$-, ($y$-, or $z$-) direction

$\alpha$ = $NH_3$/NO feed ratio

$\mu$ = viscosity

$\rho$ = gas density

## Literature Cited


Bahamonde, A., A. Beretta, P. Avila, and E. Tronconi, "An Experimental and Theoretical Investigation of the Behavior of a Monolithic Ti V W Sepiolite Catalyst in the Reduction of $NO_x$ with $NH_3$," *Ind. Eng. Chem. Res.*, **35**, 2516 (1996).

Bai, H. L., and J. W. Chwu, "Theoretical Analysis of Selective Catalytic Reduction Catalysts," *J. Environ. Eng. ASCE*, **123**, 431 (1997).

Beeckman, J. W., "Measurement of the Effective Diffusion Coefficient of Nitrogen Monoxide Through Porous Monolith-Type Ceramic Catalysts," *Ind. Eng. Chem. Res.*, **30**, 428 (1991).

Beeckman, J. W., and L. L. Hegedus, "Design of Monolith Catalysts for Power-Plant $NO_x$ Emission Control," *Ind. Eng. Chem. Res.*, **30**, 969 (1991).

Bettoni, F., "Untersuchungen zum stationären und dynamischen Verhalten eines Entstickungssystems nach dem SCR-Prinzip mit realem Dieselabgas," PhD Thesis, ETH Zurich, Switzerland (1997).

Buzanowski, M. A., and R. T. Yang, "Simple Design of Monolith Reactor for Selective Catalytic Reduction of NO for Power-Plant Emission Control," *Ind. Eng. Chem. Res.*, **29**, 2074 (1990).

Chapra, S. C., and R. P. Canale, *Numerical Methods for Engineers*, McGraw-Hill, New York (1988).

Davis, P. J., and P. Rabinowitz, *Methods of Numerical Integration*, Academic Press, New York (1984).

Duffy, B. L., H. E. Curry-Hyde, N. W. Cant, and P. F. Nelson, "Isotopic Labeling Studies of the Effects of Temperature, Water, and Vanadia Loading on the Selective Catalytic Reduction of NO with $NH_3$ over Vanadia-Titania Catalysts," *J. Phys. Chem.*, **98**, 7153 (1994a).

Duffy, B. L., H. E. Curry-Hyde, N. W. Cant, and P. F. Nelson, "The Origin of $(NH_3)$-N-15 Produced from the Reaction of $(NH_3)$-N-14 and (NO)-N-15 over Vanadia-Based SCR Catalysts," *Catal. Lett.*, **28**, 167 (1994b).

Dumesic, J. A., N. Y. Topsoe, H. Topsoe, Y. Chen, and T. Slabiak, "Kinetics of Selective Catalytic Reduction of Nitric-Oxide by Ammonia over Vanadia/Titania," *J. Catal.*, **163**, 409 (1996).

Forzatti, P., and L. Lietti, "Recent Advances in De NO(x)ing Catalysis for Stationary Applications," *Heter. Chem. Rev.*, **3**, 33 (1996).

Gerald, C. F., and P. O. Wheatley, *Applied Numerical Analysis*, 4th ed., Addison-Wesley, Reading, MA (1989).

Gilardoni, F., J. Weber, and A. Baiker, "Density-Functional Investigation of the Mechanism of the Selective Catalytic Reduction of NO by $NH_3$ over Vanadium-Oxide Model Clusters," *Int. J. Quantum Chem.*, **61**, 683 (1997a).

Gilardoni, F., J. Weber, and A. Baiker, "Mechanism of the Vanadium Oxide-Catalyzed Selective Reduction of NO by $NH_3$—A Quantum-Chemical Modeling," *J. Phys. Chem. A*, **101**, 6069 (1997b).

Groppi, G., A. Belloli, E. Tronconi, and P. Forzatti, "A Comparison of Lumped and Distributed Models of Monolith Catalytic Combustors," *Chem. Eng. Sci.*, **50**, 2705 (1995).

Han, L. S., "Hydrodynamic Entrance Length for Incompressible Laminar Flow in Rectangular Ducts," *J. Appl. Mech.*, **27**, 403 (1960).

Hawthorn, R. D., "Afterburner Catalysts—Effects of Heat and Mass Transfer Between Gas and Catalyst Surface," *AIChE Symp. Ser.*, **70**, 428 (1974).

Hayes, R. E., S. T. Kolaczkowski, W. J. Thomas, and J. Titiloye, "Intraphase Diffusion and Interphase Mass-Transfer Effects During the Catalytic-Oxidation of CO in a Tube Wall Reactor," *Proc. R. Soc. Lond. A*, **448**, 321 (1995).

Heinisch, R., A. Rogowski, and E. Schütt, "Stoffaustausch im Wabenrohrreaktor," *Chem. Ing. Tech.*, **64**, 1038 (1992).

Hu, S. L., and T. M. Apple, "N 15 NMR Study of the Adsorption of NO and $NH_3$ on Titania Supported Vanadia Catalysts," *J. Catal.*, **158**, 199 (1996).

Hwang, G. J., and J. P. Sheu, "Effect of Radial Velocity Component on Laminar Forced Convection in Entrance Region of a Circular Tube," *Int. J. Heat Mass Transfer*, **17**, 372 (1974).

Inomata, M., A. Miyamoto, and Y. Murakami, "Mechanism of the Reaction of NO and $NH_3$ on Vanadium-Oxide Catalyst in the Presence of Oxygen Under the Dilute Gas Condition," *J. Catal.*, **62**, 140 (1980).

Kumthekar, M. W., and U. S. Ozkan, "Use Isotopic Transient Techniques in the Study of NO Reduction Reactions," *Appl. Catal. A: General*, **151**, 289 (1997).

Langhaar, H., "Steady Flow in the Transition Length of a Straight Tube," *J. Appl. Mech.*, **9**, 55 (1942).

Leung, D., R. E. Hayes, and S. T. Kolaczkowski, "Diffusion Limitation Effects in the Washcoat of a Catalytic Monolith Reactor," *Can. J. Chem. Eng.*, **74**, 94 (1996).

Lietti, L., P. Forzatti, and F. Bregani, "Steady State and Transient Reactivity Study of $TiO_2$ Supported $V_2O_5$ $WO_3$ $DeNO_x$ Catalysts: Relevance of the Vanadium Tungsten Interaction on the Catalytic Activity," *Ind. Eng. Chem. Res.*, **35**, 3884 (1996).

Ozkan, U. S., Y. Cai, and M. W. Kumthekar, "Investigation of the Reaction Pathways in Selective Catalytic Reduction of NO with $NH_3$ over $V_2O_5$ Catalysts: Isotopic Labeling Studies Using $^{18}O_2$, $^{15}NH_3$, $^{15}NO$, and $^{15}N^{18}O$," *J. Catal.*, **149**, 390 (1994).

Pinaeva, L. G., A. P. Suknev, A. A. Budneva, E. A. Paukshtis, and B. S. Balzhinimaev, "On the Role of Oxygen in the Reaction of NO Reduction by $NH_3$ over Monolayer $V_2O_5$ $TiO_2$ Catalyst," *J. Mol. Catal. A Chem.*, **112**, 115 (1996).

Ramis, G., L. Yi, and G. Busca, "Ammonia Activation over Catalysts for the Selective Catalytic Reduction of $NO_x$ and the Selective Catalytic-Oxidation of $NH_3$—An FTIR Study," *Catal. Today*, **28**, 373 (1996).

Roduit, B., A. Wokaun, and A. Baiker, "Global Kinetic Modeling of Reactions Occurring During Selective Catalytic Reduction of NO by $NH_3$ over Vanadia/Titania Based Catalysts," *Ind. Eng. Chem. Res.*, in press (1998).

Schlichting, H., *Boundary Layer Theory*, 7th ed., McGraw-Hill, New York (1979).

Schlünder, E. U., *Einführung in die Wärme-und Stoffübertragung*, Vieweg, Braunschweig, Germany (1972).

Schneider, H., S. Tschudin, M. Schneider, A. Wokaun, and A. Baiker, "In-Situ Diffuse-Reflectance FTIR Study of the Selective Catalytic Reduction of NO by $NH_3$ over Vanadia-Titania Aerogels," *J. Catal.*, **147**, 5 (1994).

Scraton, R. E., *Further Numerical Methods in BASIC*, Arnold, London (1987).

Srnak, T. Z., J. A. Dumesic, B. S. Clausen, E. Tornqvist, and N. Y. Topsoe, "Temperature-Programmed Desorption Reaction and Insitu Spectroscopic Studies of Vanadia Titania for Catalytic Reduction of Nitric-Oxide," *J. Catal.*, **135**, 246 (1992).

Topsoe, N. Y., "Characterization of the Nature of Surface Sites on Vanadia Titania Catalysts by FTIR," *J. Catal.*, **128**, 499 (1991).

Topsoe, N. Y., "Mechanism of the Selective Catalytic Reduction of Nitric-Oxide by Ammonia Elucidated by in-Situ Online Fourier-Transform Infrared-Spectroscopy," *Science*, **265**, 1217 (1994).

Topsoe, N. Y., H. Topsoe, and J. A. Dumesic, "Vanadia-Titania Catalysts for Selective Catalytic Reduction (SCR) of Nitric-Oxide by Ammonia. 1. Combined Temperature-Programmed in-Situ FTIR and Online Mass-Spectroscopy Studies," *J. Catal.*, **151**, 266 (1995a).

Topsoe, N. Y., J. A. Dumesic, and H. Topsoe, "Vanadia-Titania Catalysts for Selective Catalytic Reduction of Nitric-Oxide by Ammonia. 2. Studies of Active-Sites and Formulation of Catalytic Cycles," *J. Catal.*, **151**, 241 (1995b).

Tronconi, E., "Interaction Between Chemical-Kinetics and Transport Phenomena in Monolithic Catalysts," *Catal. Today*, **34**, 421 (1997).

Tronconi, E., and P. Forzatti, "Adequacy of Lumped Parameter Models for SCR Reactors with Monolith Structure," *AIChE J.*, **38**, 201 (1992).

Tronconi, E., P. Forzatti, J. P. Martin, J. P. Gomez, and S. Malloggi, "Selective Catalytic Removal of $NO_x$—A Mathematical-Model for Design of Catalyst and Reactor," *Chem. Eng. Sci.*, **47**, 2401 (1992).

Uberoi, M., and C. J. Pereira, "External Mass Transfer for Monolith Catalysts," *Ind. Chem. Eng. Res.*, **35**, 113 (1996).

Ullah, U., S. P. Waldram, C. J. Bennett, and T. Truex, "Monolithic Reactors—Mass-Transfer Measurements Under Reacting Conditions," *Chem. Eng. Sci.*, **47**, 2413 (1992).

Van Dyke, M., "Entry Flow in a Channel," *J. Fluid Mech.*, **44**, 813 (1970).
VDI-Wärmeatlas, 6th ed., VDI-Verlag, Düsseldorf (1992).
Votruba, J., O. Mikus, K. Nguen, V. Hlavacek, and J. Skrivanek, "Heat and Mass Transfer in Honeycomb Catalysts," *Chem. Ing. Sci.*, **30**, 201 (1975).

## Appendix A: Numerical Method for Concentration Distribution in the Catalyst Wall

The scheme of the grid-point distribution applied in domain A to calculate the concentration distribution is presented in Figure 2. The function of the mass-balance equation (Eq. A1):

$$D_e\left(\frac{\partial^2 p_S}{\partial x^2}+\frac{\partial^2 p_S}{\partial y^2}\right)=R^* \tag{A1}$$

in the upper right corner of domain A is specific; therefore, the grid-point distribution must be chosen with variable step lengths. Generation of adaptive meshes allows us to achieve the desired resolution in localized regions. Grid points are added in regions of high gradients to generate a denser mesh in that region, and subtracted from regions where the solution is decaying or flattening out.

Let us choose $n$ to satisfy the following conditions (Figure 2):

$$h+kh+k^2h+k^3h+\cdots+k^nh<1 \tag{A2}$$

$$h+kh+k^2h+k^3h+\cdots+k^nh+k^{n+1}h>1. \tag{A3}$$

After computing a series expansion of the preceding equations with respect to the variable $k$, we obtain:

$$1+k+k^2+k^3+\cdots+k^n=\frac{k^{n+1}-1}{k-1} \tag{A4}$$

$$\Rightarrow h\,\frac{k^{n+1}-1}{k-1}<1. \tag{A5}$$

Taking the natural logarithm, we can solve the preceding inequality (Eq. A5) for $n$ and round the obtained value to the nearest integer toward minus infinity:

$$n=\left[\ln\left(\frac{k-1}{h}+1\right)\Big/\ln(k)\right]-1. \tag{A6}$$

The partial-pressure profile for NO can be expressed by substituting finite-difference approximations. We can compute the Taylor series of the second derivatives, with respect to variables $x$ and $y$, up to the order 3. The series data structure represents an expression as a truncated series in one indeterminate node, calculated for the particular point $(i,j)$ (see Figure 2).

$$p_{NOi,j}=p_{NO}(x,y) \tag{A7}$$

$$p_{NOi+1,j}=p_{NO}(x+ah,y)=p_{NO}(x,y)+ah\frac{\partial p_{NO}}{\partial x}(x,y)+a^2\frac{h^2}{2}\frac{\partial^2 p_{NO}}{\partial x^2}(x,y)+O_1(h^3) \tag{A8}$$

$$p_{NOi-1,j}=p_{NO}(x-bh,y)=p_{NO}(x,y)-bh\frac{\partial p_{NO}}{\partial x}(x,y)+b^2\frac{h^2}{2}\frac{\partial^2 p_{NO}}{\partial x^2}(x,y)+O_2(h^3) \tag{A9}$$

$$p_{NOi,j+1}=p_{NO}(x,y+b'h)=p_{NO}(x,y)+b'h'\frac{\partial p_{NO}}{\partial y}(x,y)+b'^2\frac{h'^2}{2}\frac{\partial^2 p_{NO}}{\partial y^2}(x,y)+O_3(h'^3) \tag{A10}$$

$$p_{NOi,j-1}=p_{NO}(x,y-a'h)=p_{NO}(x,y)-a'h'\frac{\partial p_{NO}}{\partial y}(x,y)+a'^2\frac{h'^2}{2}\frac{\partial^2 p_{NO}}{\partial y^2}(x,y)+O_4(h'^3). \tag{A11}$$

Combining Eqs. A8 and A9 and Eqs. A10 and A11, we obtain:

$$bp_{NOi+1,j}+ap_{NOi-1,j}=(a+b)\,p_{NOi,j}+\frac{h^2}{2}ab(a+b)\frac{\partial^2 p_{NOi,j}}{\partial x^2} \tag{A12}$$

$$a'p_{NOi,j+1}+b'p_{NOi,j-1}=(a'+b')p_{NOi,j}+\frac{h'^2}{2}a'b'(a'+b')\frac{\partial^2 p_{NOi,j}}{\partial x^2} \tag{A13}$$

with

$$h'=h \tag{A14}$$

$$\frac{\partial^2 p_{NOi,j}}{\partial x^2}=\frac{2\left(bp_{NOi+1,j}+ap_{NOi-1,j}-(a+b)p_{NOi,j}\right)}{h^2ab(a+b)} \tag{A15}$$

$$\frac{\partial^2 p_{NOi,j}}{\partial y^2}=\frac{2\left(b'p_{NOi,j-1}+a'p_{NOi,j+1}-(a'+b')p_{NOi,j}\right)}{h^2a'b'(a'+b')}. \tag{A16}$$

Equation A1 describing the partial-pressure profile for the reactant inside the catalyst wall can now be expressed by finite-difference approximations, that is, Eqs. A15 and A16, for the second derivates. It gives for NO:

$$\frac{1}{a(a+b)}p_{NOi+1,j}+\frac{1}{b(b+a)}p_{NOi-1,j}+\frac{1}{a'(a'+b')}p_{NOi,j-1}+\frac{1}{b'(a'+b')}p_{NOi,j+1}-\left(\frac{1}{ab}+\frac{1}{a'b'}\right)p_{NOi,j}+R^*\frac{h^2}{2D_e}=0, \tag{A17}$$

where the boundary conditions in discretized form are:

- Boundaries (I to III, Figure 2)—symmetry axis:

$$p_{NOi,j} = p_{NOi+1,j+1}, \quad \text{(A18)}$$

$$p_{NOi+1,j} = p_{NOi-1,j}, \quad \text{(A19)}$$

$$p_{NOi,j+1} = p_{NOi,j-1}. \quad \text{(A20)}$$

- Boundary (IV, Figure 2)—comparison of fluxes:

$$D_e \frac{p_{NOi,j} - p_{NOi-1,j}}{ah} + D_g \frac{p_{NOi+1,j} - p_{NOi,j}}{ah}. \quad \text{(A21)}$$

## Appendix B: Numerical Method (ADI) for Concentration Distribution in the Channel

The applied 3-D mesh can be divided into a series of $n$ mesh planes each having $i \times j$ elements. The choice of a suitable step in the $z$-direction for the calculation is governed by the stability criterion of Davis and Rabinowitz (1984). The grid points are moved in such a way that the numerical stability is fulfilled. The presence of the adaptive mesh algorithm applied may increase the number of steps needed in the $z$-direction but preserves the convergence. For the following system of partial differential equations:

$$\begin{cases} \dfrac{\partial p_{NO}}{\partial z} = \dfrac{D_g}{u_z(x,y,z)} \left( \dfrac{\partial^2 p_{NO}}{\partial x^2} + \dfrac{\partial^2 p_{NO}}{\partial y^2} \right) & \text{(B1a)} \\ \dfrac{\partial p_{NH_3}}{\partial z} = \dfrac{D_g}{u_z(x,y,z)} \left( \dfrac{\partial^2 p_{NH_3}}{\partial x^2} + \dfrac{\partial^2 p_{NH_3}}{\partial y^2} \right), & \text{(B1b)} \end{cases}$$

each axial increment is executed in two steps. Thus for NO, for the first step, from $p^n_{NO}$ to $p^{n+1/2}_{NO}$, Eq. B1a can be approximated by

$$\frac{p^{n+1/2}_{NOi,j} - p^n_{NOi,j}}{\Delta z/2} = \frac{D_g}{u_z(x,y,z)} \left( \frac{p^n_{NOi-1,j} - 2p^n_{NOi,j} + p^n_{NOi+1,j}}{(\Delta x)^2} + \frac{p^{n+1/2}_{NOi,j-1} - 2p^{n+1/2}_{NOi,j} + p^{n+1/2}_{NOi,j+1}}{(\Delta y)^2} \right). \quad \text{(B2)}$$

The approximation of $\partial^2 p_{NO}/\partial x^2$ (Eq. B2) is written explicitly (from $\partial^2 p_{NO}/\partial x^2$ at the start), that is, at the base point $p^n_{NO}$ where the values of the partial pressure are known. Consequently, only three partial-pressure terms in the approximation of $\partial^2 p_{NO}/\partial y^2$ are unknown. For the case of a square grid $(\Delta x = \Delta y)$ with $\lambda(x,y,z) = k\Delta z/\Delta x^2$ and $k = D_g/u_z(x,y,z)$, Eq. B2 can be expressed as

$$\begin{aligned} &- \lambda(x,y,z) p^{n+1/2}_{NOi,j-1} + 2(1+\lambda(x,y,z)) p^{n+1/2}_{NOi,j} \\ &\quad - \lambda(x,y,z) p^{n+1/2}_{NOi,j+1} = \lambda(x,y,z) p^n_{NOi-1,j} \\ &\quad + 2(1-\lambda(x,y,z)) p^n_{NOi,j} + \lambda(x,y,z) p^n_{NOi+1,j}, \end{aligned} \quad \text{(B3)}$$

which results in a tridiagonal set of simultaneous equations.

For the second step, from $p^{n+1/2}_{NO}$ to $p^{n+1}_{NO}$, Eq. B1a can be approximated by

$$\frac{p^{n+1}_{NOi,j} - p^{n+1/2}_{NOi,j}}{\Delta z/2} = \frac{D_g}{u_z(x,y,z)} \left( \frac{p^{n+1}_{NOi-1,j} - 2p^{n+1}_{NOi,j} + p^{n+1}_{NOi+1,j}}{(\Delta x)^2} + \frac{p^{n+1/2}_{NOi,j-1} - 2p^{n+1/2}_{NOi,j} + p^{n+1/2}_{NOi,j+1}}{(\Delta y)^2} \right). \quad \text{(B4)}$$

In contrast to the first step (Eq. B2), the approximation of $\partial^2 p_{NO}/\partial x^2$ (Eq. B4) is now implicit (from $\partial^2 p_{NO}/\partial x^2$ at the end). Thus, the bias introduced by the first step is partially corrected by the second step. For a square grid, the second step can be written as:

$$\begin{aligned} &- \lambda(x,y,z) p^{n+1}_{NOi-1,j} + 2(1+\lambda(x,y,z)) X^{n+1}_{NOi,j} \\ &\quad - \lambda(x,y,z) p^{n+1}_{NOi+1,j} = \lambda(x,y,z) p^{n+1/2}_{NOi,j-1} \\ &\quad + 2(1-\lambda(x,y,z)) p^{n+1/2}_{NOi,j} + \lambda(x,y,z) p^{n+1/2}_{NOi,j+1}. \end{aligned} \quad \text{(B5)}$$

Once the two first steps are calculated, from $p^n_{NO}$ to $p^{n+1}_{NO}$, the parabolic equation for $p_{NH_3}$ is calculated using the same procedure.

For the first step, from $p^n_{NH_3}$ to $p^{n+1/2}_{NH_3}$, we have

$$\begin{aligned} &- \lambda(x,y,z) p^{n+1/2}_{NH_3i,j-1} + 2(1+\lambda(x,y,z)) p^{n+1/2}_{NH_3i,j} \\ &\quad - \lambda(x,y,z) p^{n+1/2}_{NH_3i,j+1} = \lambda(x,y,z) p^n_{NH_3i-1,j} \\ &\quad + 2(1-\lambda(x,y,z)) p^n_{NH_3i,j} + \lambda(x,y,z) p^n_{NH_3i+1,j} \end{aligned} \quad \text{(B6)}$$

and for the second step, from $p^{n+1/2}_{NH_3}$ to $p^{n+1}_{NH_3}$, we can write

$$\begin{aligned} &- \lambda(x,y,z) p^{n+1}_{NH_3i-1,j} + 2(1+\lambda(x,y,z)) X^{n+1}_{NH_3i,j} \\ &\quad - \lambda(x,y,z) p^{n+1}_{NH_3i+1,j} = \lambda(x,y,z) p^{n+1/2}_{NH_3i,j-1} \\ &\quad + 2(1-\lambda(x,y,z)) p^{n+1/2}_{NH_3i,j} + \lambda(x,y,x) p^{n+1/2}_{NH_3i,j+1}. \end{aligned} \quad \text{(B7)}$$

Explicit methods are subject to step restriction for reasons of numerical stability. The choice of a suitable step in the $z$-direction for the calculation is governed by the stability criterion. For this type of equation, Davis (Davis and Rabinowitz, 1984) established that:

$$\Delta z \le \frac{1}{8} \left( \frac{(\Delta x)^2 + (\Delta y)^2}{k} \right),$$

where

$$k = \frac{D_g}{u_z(x,y,z)}$$

in our case. Consequently, for a uniform grid ($\Delta x = \Delta y$):

$$\lambda = \lambda(x,y,z) = \frac{k\Delta z}{(\Delta x)^2} \leq \frac{1}{4}. \tag{B8}$$

As long as the velocity profile is not fully developed (hydrodynamic entrance length), the partial-pressure gradients move through the space with a variable front velocity. However, the value of the step "$\Delta z$" in the $z$-direction must be reduced when $\lambda$ exceeds 1/4. For each step, execution of the convergence criterion is checked for all the control volumes over the entire physical domain, and the smallest required step is used. The grid size used for these simulations was $500\times 20\times 20$. The presence of the adaptive mesh algorithm that was used in order to preserve the convergence may increase the number of steps needed in the $z$-direction. Discretization of boundary conditions I and II was given for NO (likewise $NH_3$) by Eqs. A18 and A20 (Appendix A). It is also necessary to analyze the contribution of the chemical reaction occurring inside the catalyst wall (see Figure 5, boundary III). Using Eq. 7, which shows that the gradient in the $y$-direction can be neglected if compared to the one in the $x$-direction, the results presented in Figure 3, boundary III, become:

$$\left.\frac{p_{NOi+1,j} - p_{NOi,j}}{dx}\right|_{\text{gas side}} = \frac{D_e}{D_g}\left.\frac{\partial p_{NO}}{\partial x}\right|_{\text{bulk side}} \tag{B9a}$$

$$\left.\frac{p_{NH_3i+1,j} - p_{NH_3i,j}}{dx}\right|_{\text{gas side}} = \frac{D_e}{D_g}\left.\frac{\partial p_{NH_3}}{\partial x}\right|_{\text{bulk side}}, \tag{B9b}$$

where the partial-pressure gradients of both NO and $NH_3$ on the bulk side result from the chemical reactions, whose analytical expressions have been derived in another study (Roduit et al., 1998).

Consideration of Eqs. B3 and B5 to B7 and their corresponding boundary conditions (Eqs. B9, A18, and A20) make possible the calculations of the partial pressures and corresponding gradients by considering the axial ($z$) and cross-sectional ($x$, $y$) conversion progress of both reactants (NO and $NH_3$) in the gas phase.

*Manuscript received May 5, 1998, and revision received Sept. 24, 1998.*